

Light response of pure CsI calorimeter crystals painted with wavelength-shifting lacquer

E. Frlež^{a,1}, Ch. Brönnimann^b, B. Krause^b, D. Počanić^a,
D. Renker^b, S. Ritt^{a,b}, P. L. Slocum^{a,b}, I. Supek^c, H. P. Wirtz^b

^a*Department of Physics, University of Virginia, Charlottesville, VA 22904, USA*

^b*Paul Scherrer Institute, Villigen PSI, CH-5232, Switzerland*

^c*Institute Rudjer Bošković, Bijenička 46, HR-10000 Zagreb, Croatia*

Abstract

We have measured scintillation properties of pure CsI crystals used in the shower calorimeter built for a precise determination of the $\pi^+ \rightarrow \pi^0 e^+ \nu_e$ decay rate at the Paul Scherrer Institute (PSI). All 240 individual crystals painted with a special wavelength-shifting solution were examined in a custom-build detection apparatus (RASTA—radioactive source tomography apparatus) that uses a ^{137}Cs radioactive gamma source, cosmic muons and a light emitting diode as complementary probes of the scintillator light response. We have extracted the total light output, axial light collection nonuniformities and timing responses of the individual CsI crystals. These results predict improved performance of the 3π sr PIBETA calorimeter due to the painted lateral surfaces of 240 CsI crystals. The wavelength-shifting paint treatment did not affect appreciably the total light output and timing resolution of our crystal sample. The predicted energy resolution for positrons and photons in the energy range of 10–100 MeV was nevertheless improved due to the more favorable axial light collection probability variation. We have compared simulated calorimeter ADC spectra due to 70 MeV positrons and photons with a Monte Carlo calculation of an ideal detector light response.

PACS Numbers: 87.59.F; 29.40.Mc; 24.10.Lx

Keywords: Computed tomography; Scintillation detectors; Monte Carlo simulations

¹ Corresponding author; Tel: +1-804-924-6786, fax: +1-804-924-4576, e-mail: fr-lez@virginia.edu (E. Frlež)

1 Introduction

The PIBETA detector at the Paul Scherrer Institute in Switzerland was designed for the precise measurement of the pion beta ($\pi\beta$) decay branching ratio ($\pi^+ \rightarrow \pi^0 e^+ \nu_e$) as well as for study of other rare pion and muon decays [1]. The experiment has started to take production data in the summer of 1999. The heart of the detector is the $\sim 3\pi$ sr pure cesium iodide (CsI) segmented calorimeter. In-depth knowledge of the calorimeter response to the positrons and photons in the energy range 10–100 MeV is essential in order to achieve the proposed accuracy of the branching ratio measurements of $\sim 0.5\%$. Experimental signature of a $\pi\beta$ event is determined by the prompt decay $\pi^0 \rightarrow \gamma\gamma$. The $(1.025 \pm 0.034) \times 10^{-8}$ pion beta decay branching ratio [2] will be remeasured relative to the 10^4 times more probable $\pi^+ \rightarrow e^+ \nu_e$ decay rate, that is known with the combined statistical and systematic uncertainty of $\sim 0.33\%$ [3,4].

The detector energy response functions were determined both experimentally, by scanning the calorimeter with the monoenergetic e^+ and γ beams, and in Monte Carlo simulations. Inputs to the simulation calculations were the average light outputs and light output nonuniformity functions for each individual calorimeter module. In this paper we describe how these input parameters, essential for a realistic Monte Carlo detector simulation, have been measured in a dedicated tomography apparatus. Section 2 details the surface treatment of the CsI scintillator crystals. Design and operation of the radioactive source scanning apparatus are explained in Sec. 3. The extracted light output parameters are discussed in Secs. 4 and 5. In Sec. 6 we explain how these parameters are used in a **GEANT**-based calculation of the calorimeter response.

2 CsI Crystal Surface Treatment

The PIBETA calorimeter consists of 240 truncated crystal pyramids with a height of 22 cm, which corresponds to 12 radiation lengths. Nine different detector shapes were required to complete the crystal sphere [5]: four irregular hexagonal truncated pyramids (we labeled them HEX-A, HEX-B, HEX-C, and HEX-D), one regular pentagonal (PENT) and two irregular half-hexagonal truncated pyramids (HEX-D1 and HEX-D2), and two trapezohedrons (VET-1, VET-2). The volumes of studied CsI crystals vary from 797 cm^3 (HEX-D1/2) to 1718 cm^3 (HEX-C).

Twentyfive pure CsI crystals were produced by Bicron Corporation facility in Newbury, Ohio. The reminder of the crystals were grown and cut in the Institute for Single Crystals (AMCRYS) in Harkov, Ukraine. The more detailed description of the PIBETA calorimeter design is given in Refs. [6] and [7].

In Fig. 1 we show the partially assembled calorimeter with front faces and wrapped side surfaces of exposed CsI modules visible inside the mechanical support structure.

The light output of each crystal, namely the average number of photoelectrons for unit energy deposition caused by ionizing charged particles, can be tuned by using the different polishing, matting and wrapping treatments of the detector surfaces. The goal of such treatments is usually to maximize the light yield thus obtaining the best energy resolution, while keeping the detector response linear irrespective of the location of the energy deposition.

Our initial treatment of the crystal surfaces involved a test sample of 74 CsI detectors and consisted of: (a) polishing the crystal surfaces with a mixture of $0.2\text{ }\mu\text{m}$ aluminum oxide powder and ethylenglycol, (b) wrapping the lateral surfaces with two layers of Teflon foil plus one layer of aluminized Mylar sheet, and (c) covering the front crystal surface with a black paper template. The crystal back surface with the glued phototube was left uncovered. We reported the predicted response of the calorimeter with all CsI modules treated in the described manner in our previous paper [7].

Further test measurements and the technical developments [8] suggested an improved optical treatment of crystal surfaces. Due to the fact that CsI is slightly hygroscopic, it is desirable to “seal” the scintillators against potential surface deterioration and thus minimize changes of the detector response throughout the duration of the experiment. Traditional polishing and wrapping methods cannot ensure long term stability of the relevant scintillation parameters due to the insufficient chemical resistance of alkali halides [9]. Furthermore, a suitable protective coating of the crystal surfaces can at the same time be used to modulate the scintillator light collection properties and can be easily removed, if necessary.

We therefore decided to paint the surfaces of every CsI crystal using a special organosilicon mixture. The solution was developed at the Harkov Single Crystals Research Institute [10]. For our purposes the most useful polymers were polyphenylsiloxanes due to their high thermal stability, good radiation resistance and the moisture-proof quality. The optical properties of the organosilicon coatings depend on the nature of the organic radicals. Their phenyl polymer bonds can efficiently transfer the energy to the luminescent admixtures [11]. The selected polymers and solvents have a nonpolar character resulting in a low moisture absorption. On the other hand, the high optical transparency of the varnishes was achieved in a purification process by the absorption trapping of silica, aluminum oxide and hydroxide impurities. The resulting absorption and reemission of light by the coating in the wavelength range above 300 nm was better than 99%.

Specifically, the waveshift lacquer was the ladder organosilicon copolymer with the chemical composition PPO+POPOP+COUM.1, where PPO is 2,5-Diphenyloxazole, POPOP represents 1,4-Di-2-(5-Phenyloxazolyl)-Benzene and COUM.1 is 7-Diethylamine-4-Methylcoumarin [12]. That paint solution was applied twice resulting in a protective cover with a total thickness of 120 μm . The dried paint layer has the index of refraction $n_D=1.62$ and the density $\rho=1.094$, and is soluble in ethyl alcohol. Following the paint application each detector module was wrapped in two layers of a 38 μm PTFE Teflon sheet and two layers of 20 μm thick aluminized Mylar to make it optically insulated from its calorimeter neighbors.

We have compared the average fast-to-total (F/T) analog signal ratio and the photoelectron statistics of all lacquer-treated crystals with the measurements of polished and Teflon-wrapped crystals we reported on in Ref. [7]. The F/T ratio was virtually unchanged at 0.77, while the number of photoelectrons per MeV was just under 3% lower, changing from an average of 64 to 62 Photoelectrons/MeV at the ambient temperature of 18°C. The combined statistical and systematic uncertainty of these measurements was less than 1 Photoelectron/MeV.

The averaged lineshape of an analog cosmic muon signal from one CsI detector captured on a digital oscilloscope is shown in Fig. 2. The 10-to-90% amplitude rise time of the analog signal changed from 4.0 ns for the Teflon-wrapped scintillators to 4.8 ns for the lacquer-painted detectors, due to the fact that a fraction of the scintillator light is now absorbed by the wavelength-shifting surfaces and reemitted later with the different wavelength. Histograms of the F/T ratios and the photoelectron numbers for the painted crystals are shown in Figs. 3 and 4, respectively.

3 RASTA: RAdioactive Source Tomography Apparatus

The total light output and the position-dependent light collection probabilities for each CsI detector were measured in a test setup using a ^{137}Cs radioactive gamma source with an activity of 3.7 MBq. It was found that this method produced results consistent with the cosmic muon tomography [7] and was well suited for the routine crystal uniformity tests. Thus an apparatus was designed and built to allow a fast, precise and reproducible method of determining the optical nonuniformity of each CsI crystal.

The drawing of the main parts of the apparatus is shown in Fig. 5. The ^{137}Cs radioactive gamma source was embedded in a lead collimator. The collimator had a thickness of 5 cm while its pin-hole had a diameter of 6 mm. The probability for the 0.662 MeV ^{137}Cs photons to penetrate that lead thickness

is $< 1\%$. The ionization energy deposited at the central axis of a CsI crystal is about one-sixth of the energy deposition near the crystal surface. The collimator was mounted on an aluminum plate, which was moved by a stepping motor. The precision of the step motor movements was $12.5\,\mu\text{m}$. The examined crystal was placed on a horizontal aluminum plate using a dedicated positioning system with a precision of $\sim 0.3\text{ mm}$. The stepping motor was controlled by a PC486 personal computer through a RS232 interface.

The schematic diagram of the logic electronics is shown in Fig. 6. The analog photomultiplier signal was amplified by a factor of 10 using an LRS 612A photomultiplier amplifier. The signal was then split, one copy going into the trigger logic while the other copy was delayed and fed into an LRS 2249A CAMAC ADC. The trigger created a computer LAM in the SIN IO506 input/output unit. The CAMAC modules were controlled using a HYTEC 1331 Turbo CAMAC-PC interface.

The stability of the system after switching on the PMT high voltage was studied in preliminary calibrations. The data were taken with a CsI crystal in a fixed position every 5 minutes and the results are shown in Fig. 7. We concluded that the PMT high voltage should be switched on for at least one hour before doing any measurements with the detector.

A full calibration was performed on each CsI crystal by scanning it four times within three hours. The measured light output as a function of scan position are shown in Fig. 8 for the CsI detector number S040. After the cross-normalization the results of different measurements agreed within the 0.5% statistical uncertainty.

4 Total Light Output of the CsI Detectors

Scintillation light of a full-sized CsI crystal was read by a 78 mm diameter EMI 9821QKB photomultiplier tube with quartz photocathode window. The smaller half-sized crystals were directly coupled to a 52 mm ϕ EMI 9211QKA PMTs with similar characteristics [13]. Both phototube types were glued to the back faces of the crystals using a clear silicone elastomer Sylgard 184 manufactured by Dow Corning [14].

A light-emitting diode (LED) was attached to the exposed back side of the CsI detector. The whole detector assembly was placed in the light-tight RASTA box. The LEDs were excited at a $\sim 10\text{ Hz}$ rate using a NIM diode driver with an adjustable output voltage. The LED pulses simulated constant energy depositions in the CsI crystal corresponding to a 10–100 MeV range. The absolute energy calibration was established by comparison with measured cosmic muon

ADC spectra. These spectra were acquired in calibration runs triggered by two small plastic scintillator tag counters placed above and below the CsI crystal. Their expected peak positions, expressed in the units of MeV, were calculated in a **GEANT** Monte Carlo simulation.

For LED measurements the variance σ_E^2 of a PMT pulse-height spectrum depends upon the mean number of photoelectrons \bar{N}_{pe} from the photocathode created per unit energy deposition in the scintillator:

$$\sigma_E^2 = \sum_i \sigma_i^2 + \bar{E}/\bar{N}_{pe}, \quad (1)$$

where \bar{E} is the spectrum peak position and σ_i^2 's are assorted variances, such as the instabilities of LED driving voltage and temporal ADC pedestal variations.

The energy resolutions σ_E 's were measured for 9 different values of the LED driving voltage and the photoelectron numbers \bar{N}_{pe} were calculated by the least-squares fit using Eq. (1). The mean numbers of photoelectrons normalized to the unit equivalent-energy deposition in MeV and scaled down the ambient temperature of 18°C are shown in Fig. 4. The histograms for the full-sized crystals and half-sized crystals are displayed separately, with the ratio of 2.4 in photoelectron statistics essentially consistent with the surface area ratio of 2.25 in the two differently-sized photocathodes.

5 Spatial Light Output Nonuniformity of the CsI Detectors

The 3-dimensional spatial distribution of scintillation light output can be specified by giving the number of photoelectrons $N_{pe}(x, y, z)$ produced by a 1 MeV energy deposition at the point (x, y, z) ("3-dimensional light nonuniformity function"). In the following discussion we limit ourselves to the linear and one-dimensional variation of the detected light output $N_{pe}(z)$ along the long axis of the detector:

$$N_{pe}(z) \propto \begin{cases} N_1 + a_{z1} \cdot z & 0 \leq z \leq 10 \text{ cm}, \\ N_2 + a_{z2} \cdot z & 10 \leq z \leq 18 \text{ cm}, \\ N_3 + a_{z3} \cdot z & 18 \leq z \leq 22 \text{ cm} \end{cases} \quad (2)$$

where a_z 's are the linear optical nonuniformity coefficients in the axial coordinate z , and the coordinate system origin is at the center of the detector front face. In this approximation the transverse light output variations are integrated away. In our figures and tables we are quoting the a_z light nonuniformity parameters in units of %/cm.

The complete RASTA database of all 240 studied CsI crystals is made available for online inspection at the PIBETA WWW site [15]. The measurements for each CsI crystal are summarized on separate WWW pages. Individual pages start with the pulse-height spectra recorded with the cosmic muon trigger that is used for the absolute energy calibration of the ADC scale. The LED “energy” spectra corresponding to 9 different LED intensities are shown next, together with the superimposed Gaussian fits. The least-square linear fits of the data using the Eq. (1), which allow the deduction of the average number of photoelectrons per MeV, as well as the associated fit uncertainties, are documented below the spectra. The timing resolution histogram is also presented; it gives the standard deviation of the CsI detector timing spectrum with respect to the tag counters TDC value for the cosmic muon triggers.

Also displayed are the ADC spectra taken with the ^{137}Cs radioactive source at 11 equidistant positions along the long axis of a studied crystal, together with Gaussian-exponential fits. The fitted Gaussian peak positions are plotted in the axial light nonuniformity figures that follow next. The relative axial variations of the light collection nonuniformities are shown for 6 representative CsI crystals in Fig. 9. The extracted linear nonuniformity coefficients a_z ’s are listed last.

The relation between the linear nonuniformity coefficients a_{z1} in the front part of the crystal ($z \leq 10$ cm) and the coefficients a_{z2} describing the position-dependent change of the axial light output in the central and back crystal part is shown on the scatter plot in Fig. 10 for all 240 crystals. Fig. 11 compares the linear function $a_{z2} = c_1 + c_2 \cdot a_{z1}$ fitted to the scatter plot with the result deduced from our previous measurements of the Teflon-wrapped crystals, Ref. [7]. The parameters c_1 and c_2 were determined by the “robust” estimation method [16] by imposing the requirement of the minimum absolute deviation between the measured and calculated values. The treatment of crystal surfaces with the wavelength-shifting lacquer produces more favorable light output collection along the detector axis by increasing the collected light from the back part of a crystal and thus compensating for the energy leakage of electromagnetic showers and improving the detector energy resolution. These results were confirmed in the full-fledged **GEANT** simulation described in Sec 6.

In Fig. 12 we show the timing resolutions for the all measured CsI crystals. We have histogrammed the standard deviations of the Gaussian functions fitted to the spectrum of the timing differences between the CsI detector and the small scintillator tag counter just above the crystal. The average CsI detector timing uncertainty specified in such a way is 0.68 ns.

We have summarized the average scintillation properties of all 240 studied CsI crystals in Tables 1 and 2.

6 Simulated ADC Lineshapes of 70 MeV/c e^\pm 's and γ 's

We have developed a comprehensive **GEANT** Monte Carlo description of the PIBETA detector that includes all major active as well as passive detector components [17]. The user code is written in a modular form in standard **FORTRAN** and organized into over 300 subroutines and data files [18]. The graphical user interface to the code based on **Tcl** routines supplements the program.

Standard **GEANT** routines account for electromagnetic shower processes in **CsI**: leak-through, lateral spreading, backsplash, as well as the electromagnetic interactions in the active target and tracking detectors: bremsstrahlung, Bhabha scattering, in-flight annihilation for positrons, and pair production, Compton scattering, etc. for photons.

The individual PIBETA detector components, both passive and active ones, can be positioned or “switched off” without recompiling the code. The following detectors are defined in the Monte Carlo geometry:

- (1) a beam counter, an active plastic scintillator degrader and several versions of segmented stopping active targets;
- (2) two concentric cylindrical multiwire proportional chambers used for charged particle tracking;
- (3) a 20-piece cylindrical plastic scintillator hodoscope used for charged particle detection and discrimination;
- (4) a 240-module pure **CsI** calorimeter sphere;
- (5) a 5-plate cosmic muon veto scintillator system;
- (6) passive calorimeter support structure and the individual detector support systems,
- (7) the detector phototubes and HV divider bases, and the lead brick shielding structure.

User input to the simulation code requires the detector version, e.g., the run year, the beam properties, the selected reaction/decay final states, and the version of the ADC and TDC simulation codes. User can select one particular final state or any combination of different final states with the relative probabilities defined by the reaction cross sections and decay branching ratios. The simulation of ADC values and TDC hits takes into account the individual detector photoelectron statistics, the axial and transverse light collection detector nonuniformities, ADC pedestal variations, electronics noise, and the event pile-up effects. The photoelectron statistics and the individual detector light collection nonuniformity coefficients are initialized from the **RASTA** database file. Calculation of accidental coincidences up to the fourth order is optional.

Selectable options also include the effects of:

- (1) lateral and axial extent and the divergences of the stopping pion beam;
- (2) positron and muon beam contamination;
- (3) photonuclear and electron knockout reactions in CsI material [19];
- (4) aluminized Mylar wrapping of CsI modules and plastic scintillator veto staves;
- (5) cracks between the CsI detector modules;
- (6) temperature coefficients of the individual calorimeter modules;
- (7) gain instability of the calorimeter detector modules;
- (8) electronics discriminator thresholds and ADC gate width.

Particular attention was paid to the correct accounting of “software gains” for the individual CsI modules. In the simulation calculation the values of the detector software gains allow the same user control element as the detector high voltages in the operation of the physical detector. The software gains are determined in an iterative procedure constrained by the Monte Carlo $\pi \rightarrow e^+ \nu$ positron ADC spectra in each CsI detector. Namely, in the real experiment the high voltages of the individual CsI detectors are also set by matching the positions of the 69.8 MeV positron peaks.

The output of the calculation provides the selected experimental layout and the final states chosen in the calculation, as well as the used production cross sections and branching ratios. A number of physical variables that could be of interest to a user are histogrammed in 1- and 2-dimensional format. Raw-wise and column-wise PAW Ntuples [20] are used to digitize the individual events. Simulated energy depositions and the ADC and TDC values associated with the active detectors are saved on an event-per-event basis. A single event display program can be used to examine in detail the particular event in an output stream.

Simulated calorimeter ADC spectra for 69.8 MeV monoenergetic positrons and 70.8 MeV photons generated in the stopping target are shown in Fig. 13. The figure shows the ADC lineshapes summed over all 220 calorimeter signals that make up the low threshold ($E_{\text{THR}} > 5$ MeV) trigger logic. The top panel shows the spectra without the energy cut on the 20 summed veto CsI signals that define the beam opening/exit calorimeter surfaces, the bottom panel shows the same spectra with the imposed veto energy cut. Fig. 14 displays the same variables but now summed only over the calorimeter detector with the maximum energy deposition and its nearest neighbors. That restricted ADC sum should reduce the contribution of accidental event pile-up to the smearing of the energy spectra.

The e^+ and γ peak positions, their widths and tail fractions of the simulated ADC lineshapes are summarized in Tables 3 and 4. We see that the calorimeter

energy resolution is improved and the energy spectra tail fractions reduced in the detector with the paint-treated crystals. The improvement is smaller for the positron showers which deposit most of their energy close to the incident particle impact point, but is considerable, over 15 %, for the 70 MeV photons which penetrate deeper into the calorimeter.

7 Conclusion

We have measured the scintillation properties of the individual pure CsI crystals used in the PIBETA calorimeter. The crystals were treated with a special wavelength-shifting organosilicon paint. The fraction of the fast decay component in the total light output, the photoelectron statistics and the temperature dependence of the light output are documented for the each detector. A ^{137}Cs radioactive source scanning apparatus was designed and used to determine the axial light collection nonuniformity of all scintillator crystals. An individual CsI detector response was described by three linear light nonuniformity coefficients.

These experimentally determined scintillation properties of the calorimeter components provide the essential input to a comprehensive **GEANT** Monte Carlo of the PIBETA detector. We have compared the simulated performance of the PIBETA calorimeter having the waveshift-painted CsI crystals with an idealized calorimeter characterized by the uniform light collection from every volume element of the scintillator. The comparison shows that the PIBETA calorimeter made up of the painted CsI crystals has better energy resolution, while its timing resolution is not compromised.

8 Acknowledgements

This work is supported and made possible by grants from the US National Science Foundation and the Paul Scherrer Institute.

9 Appendix A. RASTA Programs

The main computer program which operated the apparatus was named RASTA. Its main tasks were to:

- (1) control the stepping motor operation;

- (2) control and read out the CAMAC modules;
- (3) perform histogram analysis including pedestal and background subtraction, histogram filling and fitting;
- (4) provide graphical data display.

Upon the execution of the program, the operator was first asked for the serial number **Sxxx** of the crystal being tomographed. A new disk subdirectory **hisxxx** was created in which all the relevant histograms of a scan process were stored.

The starting parameters of the program were defined in the file **RASTA.INI**:

```
[Scan]
Time=20
Origin=1.0
Stepsize=2.0
NumberofSteps=11
[Fit]
PeakFindMin=10.
PeakFindMax=800.
Transition=-20.0
NsigmaXLow=2.0
NsigmaXHigh=6.0
```

The category **Scan** controlled the scanning process:

- (1) **Time** is the scan time per point in seconds;
- (2) **Origin** is the starting point of the scan (with the origin marked in the drawing of the apparatus, Fig. 5);
- (3) **Stepsize** is the distance between measured points given in centimeters.

The category **Fit** executed the fitting process:

- (1) **PeakFindMin** (**PeakFindMax**) is the lower (upper) limit of the peak position passed to the fitting program when searching for the maximum ADC value and FWHM of the pulse-height spectrum;
- (2) **Transition** is the value of the Gauss-exponential transition of the fit function measured from the peak position;
- (3) **NsigmaXLow** and **NsigmaXHigh** define the histogram range to be fitted in units of the Gaussian standard deviation from the peak position.

After having changed or accepted the default run parameters the step motor was initialized and the collimator moved to the parking position where the pedestal data and background data were taken.

The crystal was then scanned automatically at the points specified in the `RASTA.INI` file. Fig. 15 shows the computer display as it appeared during the scanning process.

At the end of the scan all histograms were stored so that the data could be easily reviewed in a Microsoft **EXCEL** spreadsheet (histograms numbers 0 and 1) or with the in-house developed Histogram Manager utility [21] (histograms 2 to NSTEP+3).

Two other programs are supplied together with the **RASTA** package:

- (1) **HVSET**, which helps select the high voltage (HV) value for the photomultiplier attached to a new crystal being prepared for tomography. The additional input parameters are the HV starting value, the preset pulse-height spectrum peak value and maximum difference between the preset and fitted peak value;
- (2) **MOVE**, which allows to position the collimator at the required location.

References

- [1] D. Počanić, D. Day, E. Frlež, R. M. Marshall, J. S. McCarthy, R. C. Minehart, K. O. H. Ziock, M. Daum, R. Frosch and D. Renker, PSI R-89.01 Experiment Proposal (Paul Scherrer Institute, Villigen, 1988).
- [2] W. K. McFarlane, L. B. Auerbach, F. C. Gaille, V. L. Highland, E. Jastrzembski, R. J. Macek, F. H. Cverna, C. M. Hoffman, G. E. Hogan, R. E. Morgado and R. D. Werbeck, Phys. Rev. D32 (1985) 547.
- [3] G. Czapek, A. Federspiel, A. Fluckiger, D. Frei, B. Hahn, C. Hug, E. Hugentobler, W. Krebs, U. Moser, D. Muster, E. Ramseyer, H. Scheidiger, P. Schlatter, G. Stucki, R. Abela, D. Renker and E. Steiner, Phys. Rev. Lett. 70 (1993) 17.
- [4] D. I. Britton, S. Ahmad, D. A. Bryman, R. A. Burnham, E. T. H. Clifford, P. Kitching, Y. Kuno, J. A. Macdonald, T. Numao, A. Olin, J. M. Poutissou and M. S. Dixit, Phys. Rev. D49 (1994) 28.
- [5] H. Kenner, Geodesic Math and How to Use It (University of California Press, Berkeley, 1976).
- [6] K. A. Assamagan, Ph. D. Thesis (University of Virginia, Charlottesville, 1995) unpublished.
- [7] E. Frlež, I. Supek, K.A. Assamagan, Ch. Brönnimann, T. Flügel, B. Krause, D. W. Lawrence, D. Mzavia, D. Počanić, D. Renker, S. Ritt, P. L. Slocum, and N. Soić, *Cosmic muon tomography of pure cesium iodide calorimeter crystals*, Nucl. Inst. and Meth. A440 (2000) 57.
- [8] D. Renker, Private Communication (1995).
- [9] G.I. Britvich, V.G. Vasilchenko, A.I. Peresyarkin, V.I. Rykalin, L.D. Kornilovskaya, S.A. Malinovskaya, V.T. Skripkina, V.M. Shershukov, E.G. Yushko, A.V. Kulinichenko, and A.I. Pyshchev, Instrum. Exp. Tech. 36 (1993) 74.
- [10] V. I. Goriletsky, L. A. Andryushenko, A. M. Kudin, Private Communication, Alkali Halide Crystal Division, Institute for Single Crystals, National Academy of Sciences of Ukraine (60 Lenin Prosp., 310001 Harkov, Ukraine).
- [11] B. V. Grynov, I. A. Andryushenko, V. M. Shershukov et al., Mat. Res. Soc. Symposium Proc. Scintillator and Phospor Materials, 346 (1994) 187.
- [12] D. R. Lide, *CRC Handbook of Chemistry and Physics*, 71st Ed., p. 3-357 (CRC Press, Boca Raton, 1990).
- [13] THORN-EMI Electron Tubes Catalog: Photomultipliers and Accessories, Rockaway, NJ (1993).
- [14] Dow Corning: Silicone Encapsulants—Technical Data, accessible at <http://www.dowcorning.com>, (2000).

- [15] Ch. Brönnimann and H. P. Wirtz, RASTA Database, accessible at URL <http://pibeta.phys.Virginia.EDU/~pibeta/subprojects/rasta/database/database.htm>, (1996).
- [16] P. J. Huber, *Robust Statistics* (Wiley, New York, 1981).
- [17] R. Brun, F. Bruyant, M. Maire, A. C. McPherson and P. Zancarini, *GEANT 3.21 DD/EE/94-1* (CERN, Geneva, 1994).
- [18] E. Frlež, Complete *GEANT* Description of the PIBETA Detector, accessible at URL <ftp://pibeta.phys.Virginia.EDU> under `/pub/pibeta/geant`, (1997).
- [19] J. Ahrens et al., Nucl. Phys. A251 (1975) 478; A. Lepretre et al., Nucl. Phys. A367 (1981) 237; H. Hebach, A. Wortberg, and M. Gari, Nucl. Phys. A267 (1976) 425; B. L. Berman et al., Phys. Rev. 177 (1969) 1745; R. L. Bramblett et al., Phys. Rev. 148 (1966) 1198; G. G. Jonsson and B. Forkman, Nucl. Phys. A107 (1968) 52.
- [20] R. Brun, O. Couet, C. Vandoni, P. Zancarini and M. Goossens, *PAW 2.03—Physics Analysis Workstation CN/Q121* (CERN, Geneva, 1993).
- [21] S. Ritt, *Histogram Manager* (Paul Scherrer Institute, Villigen PSI, 1995) unpublished.

Fig. 1. Picture of the CsI calorimeter during the mechanical assembly. About half of individual crystals (of the 240 total) are seen in a self-supporting configuration inside the detector cradle.

Fig. 2. Comparison of the cosmic muon waveforms for a hexagonal CsI detector wrapped in aluminized Mylar (dashed line) and for the same crystal painted with the wavelength-shifting lacquer (full line).

Fig. 3. Histogram of the fast-to-total light component ratio for all studied CsI crystals. Light output of unwrapped painted crystals was measured with a digital oscilloscope at the average ambient temperature of 22°C.

Fig. 4. Histogram of the number of photoelectrons per MeV of deposited energy for full-sized (left panel) and half-sized (right panel) CsI detectors normalized to the ambient temperature of 18°C.

Fig. 5. Schematic drawing of the RASTA experimental apparatus. The depicted assembly is enclosed in a light-tight aluminum box with a hinged cover plate.

Fig. 6. Schematic drawing of the RASTA logic electronics. In routine data acquisition mode the trigger is provided by the discriminated single CsI detector signal.

Fig. 7. Plot of the drift and leveling off of the pulse-height spectrum peak position due to the settling down of the photomultiplier during the first hour after the PMT high voltage is switched on.

Fig. 8. Plots of the reproducibility of the axial light nonuniformity measurements demonstrated with four sets of measurements of a single CsI crystal taken consecutively.

Fig. 9. Plots of the relative light output as a function of the radioactive source axial position for six different CsI detectors. The detector phototubes are positioned at $z=22$ cm.

Fig. 10. Light nonuniformity coefficients a_{z1} and a_{z2} (%/cm), determined separately for the front ($z \leq 10$ cm) and back ($z \geq 10$ cm) crystal sections, are plotted in a scatter-plot for 240 CsI detectors. Full-sized hexagonal and pentagonal detectors are represented with full circles, while the open circles indicate the half-hexagonal and trapezoidal detector shapes.

Fig. 11. Plot of the relationship between the linear light output nonuniformity coefficients a_{z1} and a_{z2} for the polished and Teflon-wrapped CsI crystals (dotted line) and for crystals painted with the waveshift lacquer (full line).

Fig. 12. Cosmic muon timing for one representative CsI crystal with respect to the plastic scintillator tag counter (top panel) and the timing resolutions of all studied CsI crystals (bottom panel). The resolution is defined as the standard deviation of the TDC timing difference between the tag counter and the CsI detector.

Fig. 13. The predicted PIBETA calorimeter spectra for monoenergetic 69.8 MeV positrons and 70.8 MeV photons. All CsI values above the 0.5 MeV TDC threshold (excluding the 20 trapezoidal veto counters) were summed to obtain the deposited energy. The GEANT simulation used different numbers of photoelectrons/MeV and linear axial light collection nonuniformities for each crystal as extracted in the RASTA analysis. The bottom panel shows the spectrum obtained when the CsI calorimeter veto cut is applied.

Fig. 14. The predicted PIBETA calorimeter spectra for monoenergetic 69.8 MeV positrons and 70.8 MeV photons. ADC values for the CsI crystal with the maximum ADC value together with ADC readings of its nearest neighbors were summed. A GEANT simulation used different numbers of photoelectrons/MeV and linear axial light collection nonuniformities for each crystal, as measured in the RASTA apparatus. The dashed histograms represent the simulation with the software detector gains equal to 1.

Fig. 15. The RASTA computer screen display showing the fitted histograms during automated data acquisition and analysis of a single CsI crystal.

Table 1

Average scintillation properties of the painted hexagonal and pentagonal PIBETA CsI calorimeter crystals PENTAs, HEX-As, HEX-Bs, HEX-Cs and HEX-Ds (200 crystals). The light yields are normalized to the temperature of 18°C. All other parameters were measured at the average laboratory room temperature of 22°C.

	BICRON CsI	Harkov CsI
	Crystals (22)	Crystals (178)
Fast-to-Total Ratio (100 ns/1 μ s gate)	0.835	0.760
No. photoelectrons/MeV (100 ns ADC gate)	74.2	65.2
No. photoelectrons/MeV (1 μ s ADC gate)	88.8	85.8
Fast Light Temp. Coefficient (%/°C)	-1.20	-1.61
Total Light Temp. Coefficient (%/°C)	-1.35	-1.40
Axial Nonuniformity Coefficient (%/cm), $z \leq 10$ cm, 100 ns ADC gate	0.178	0.297
Axial Nonuniformity Coefficient(%/cm), $z \geq 10$ cm, 100 ns ADC gate	0.405	0.635

Table 2

Average scintillation properties of the lacquered half-hexagonal and trapezoidal PI-BETA CsI calorimeter modules HEX-D1/2s and VETO-1/2s (40 crystals). All crystals were polished and painted and wrapped in an aluminized Mylar foil afterwards.

	BICRON CsI	Harkov CsI
	Crystals (3)	Crystals (37)
Fast-to-Total Ratio (100 ns/1 μ s gate)	0.806	0.757
No. photoelectrons/MeV (100 ns ADC gate)	31.3	26.2
No. photoelectrons/MeV (1 μ s ADC gate)	38.8	34.6
Fast Light Temp. Coefficient ($\%/^{\circ}\text{C}$)	-2.08	-0.63
Total Light Temp. Coefficient ($\%/^{\circ}\text{C}$)	-1.78	-0.69
Axial Nonuniformity Coefficient ($\%/cm$), $z \leq 10$ cm, 100 ns ADC gate	0.062	0.315
Axial Nonuniformity Coefficient($\%/cm$), $z \geq 10$ cm, 100 ns ADC gate	1.592	1.735

Table 3

The predicted energy resolutions and tail contributions for 69.8 MeV e^+ and 70.8 MeV γ 's events in the full PIBETA calorimeter. The light output in photoelectrons/MeV and the linear axial light collection nonuniformities measured for individual CsI crystals ($a_{z1,z2}$ =RASTA) were used in the GEANT simulation. Values corresponding to perfect optically homogeneous crystals ($a_{z1,z2}$ =0) are shown for comparison.

Parameter	69.8 MeV e^+		70.8 MeV γ	
No E_V cut	$a_{z1,z2}=0$	RASTA $a_{z1,z2}$	$a_{z1,z2}=0$	RASTA $a_{z1,z2}$
Peak Position (MeV)	68.87 \pm 0.03	68.78 \pm 0.03	70.10 \pm 0.03	69.50 \pm 0.05
FWHM ₍₂₂₀₎ (MeV)	3.66 \pm 0.03	3.50 \pm 0.03	3.98 \pm 0.03	3.97 \pm 0.04
5 \leq Events \leq 54 MeV (%)	6.44 \pm 0.09	6.11 \pm 0.09	8.20 \pm 0.10	7.32 \pm 0.09
5 \leq Events \leq 55 MeV (%)	6.89 \pm 0.09	6.48 \pm 0.09	8.86 \pm 0.10	7.83 \pm 0.10
$E_V \leq 5$ MeV	$a_{z1,z2}=0$	RASTA $a_{z1,z2}$	$a_{z1,z2}=0$	RASTA $a_{z1,z2}$
Peak Position (MeV)	68.88 \pm 0.03	68.89 \pm 0.03	70.07 \pm 0.03	69.50 \pm 0.04
FWHM ₍₂₂₀₎ (MeV)	3.67 \pm 0.03	3.49 \pm 0.03	3.99 \pm 0.03	3.97 \pm 0.04
5 \leq Events \leq 54 MeV (%)	1.91 \pm 0.05	1.70 \pm 0.05	3.92 \pm 0.07	3.15 \pm 0.07
5 \leq Events \leq 55 MeV (%)	2.24 \pm 0.05	1.99 \pm 0.05	4.46 \pm 0.07	3.57 \pm 0.07

Table 4

The predicted energy resolutions and tail contributions for 69.8 MeV e^+ and 70.8 MeV γ events in PIBETA clusters containing the crystal with maximum energy deposition and its nearest neighbors.

Parameter	69.8 MeV e^+		70.8 MeV γ	
No E_V cut	$a_{z1,z2}=0$	RASTA $a_{z1,z2}$	$a_{z1,z2}=0$	RASTA $a_{z1,z2}$
Peak Position (MeV)	67.74 \pm 0.03	67.80 \pm 0.04	68.80 \pm 0.03	68.63 \pm 0.03
FWHM _(NN) (MeV)	5.22 \pm 0.03	5.37 \pm 0.04	6.01 \pm 0.03	5.98 \pm 0.04
5 \leq Events \leq 54 MeV (%)	3.83 \pm 0.07	3.67 \pm 0.07	5.47 \pm 0.08	4.67 \pm 0.08
5 \leq Events \leq 55 MeV (%)	4.54 \pm 0.07	4.64 \pm 0.08	6.33 \pm 0.09	5.39 \pm 0.09
$E_V \leq 5$ MeV	$a_{z1,z2}=0$	RASTA $a_{z1,z2}$	$a_{z1,z2}=0$	RASTA $a_{z1,z2}$
Peak Position (MeV)	67.75 \pm 0.03	67.76 \pm 0.03	68.80 \pm 0.04	68.60 \pm 0.04
FWHM _(NN) (MeV)	5.52 \pm 0.03	5.24 \pm 0.03	5.92 \pm 0.03	5.85 \pm 0.03
5 \leq Events \leq 54 MeV (%)	3.53 \pm 0.07	3.17 \pm 0.07	5.28 \pm 0.08	4.29 \pm 0.08
5 \leq Events \leq 55 MeV (%)	4.19 \pm 0.07	3.76 \pm 0.07	6.10 \pm 0.09	4.98 \pm 0.08

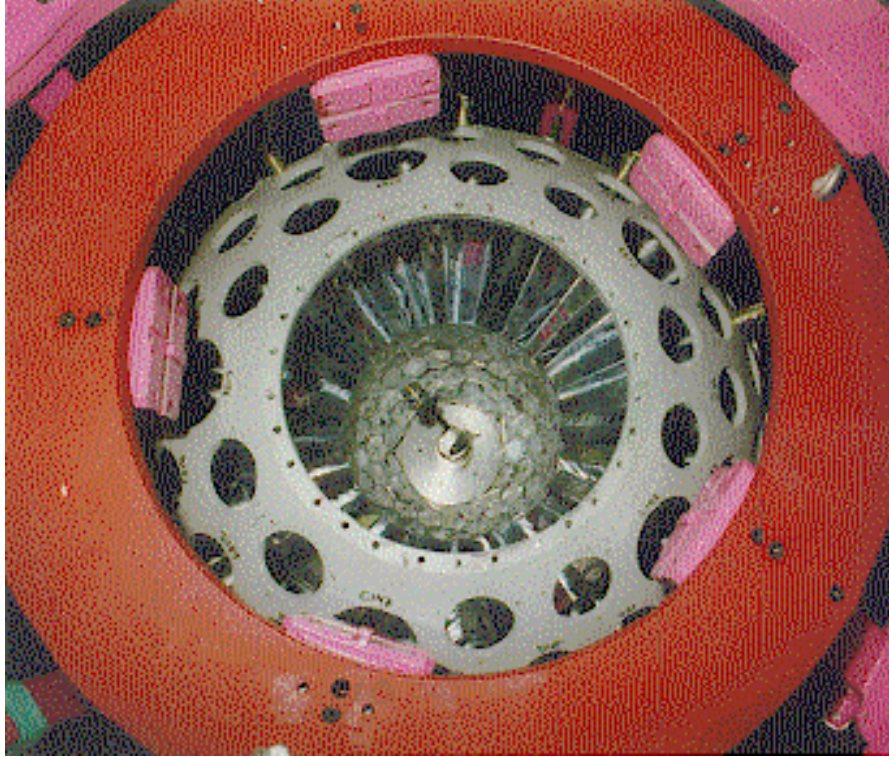


FIGURE 1

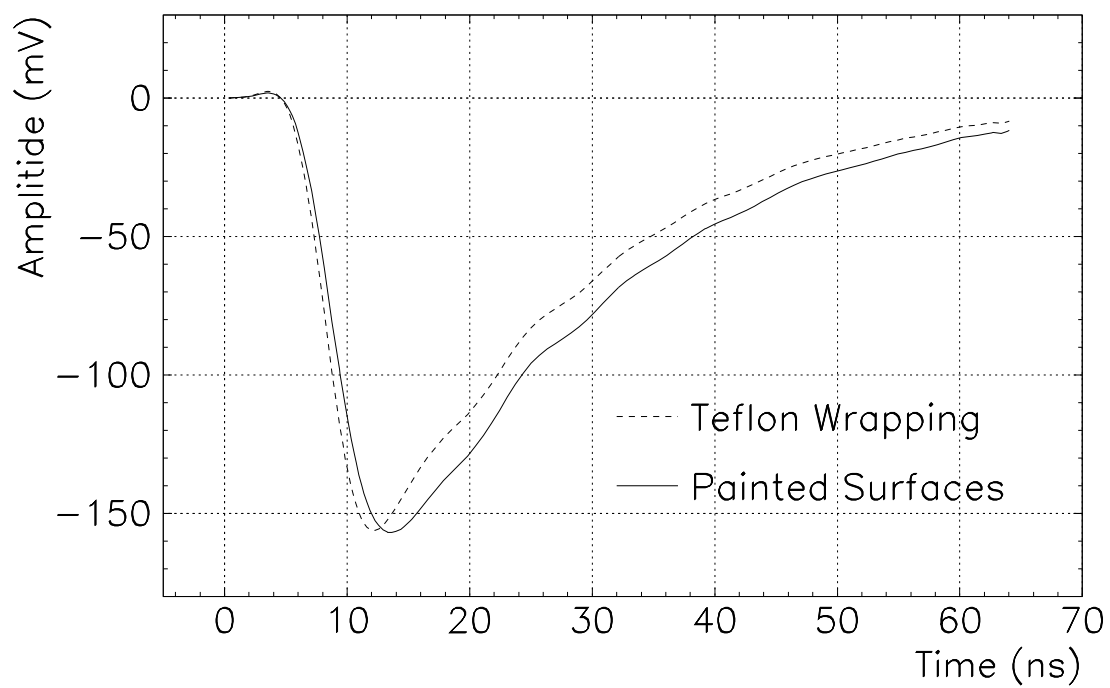


FIGURE 2

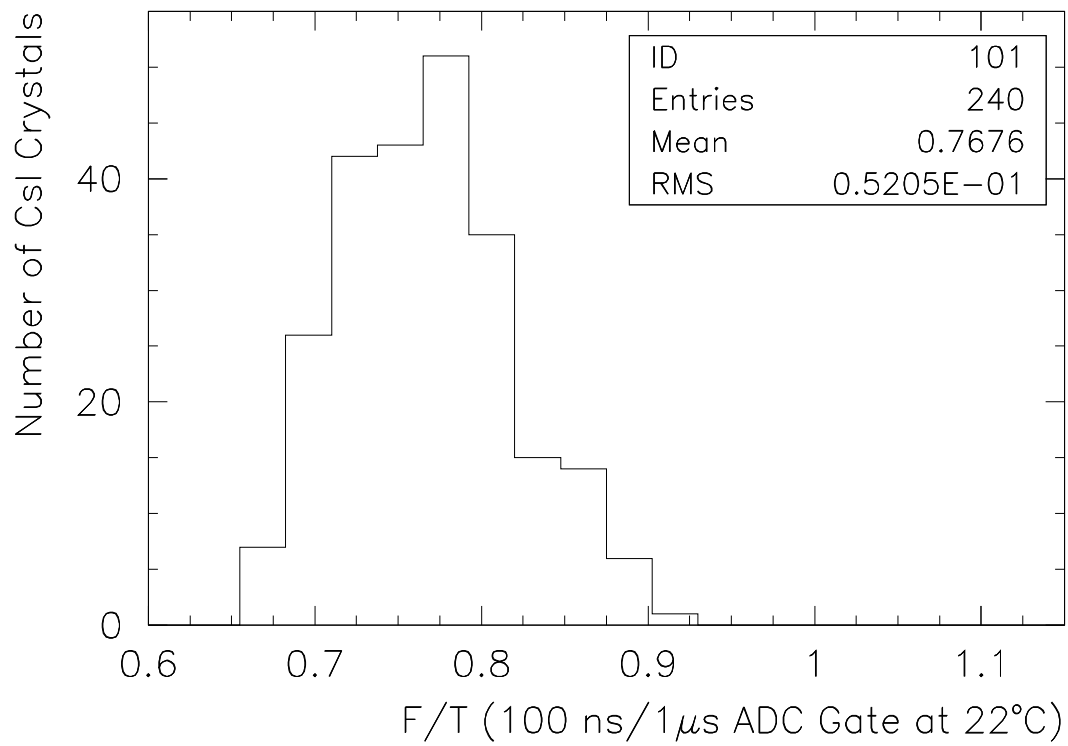


FIGURE 3

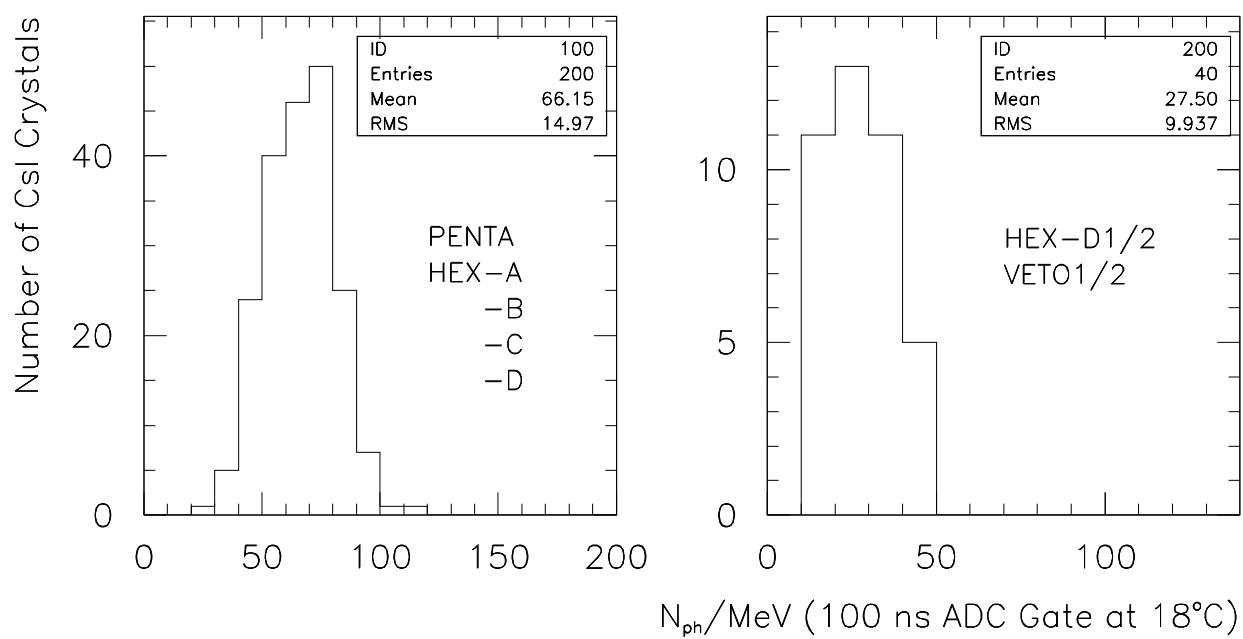


FIGURE 4

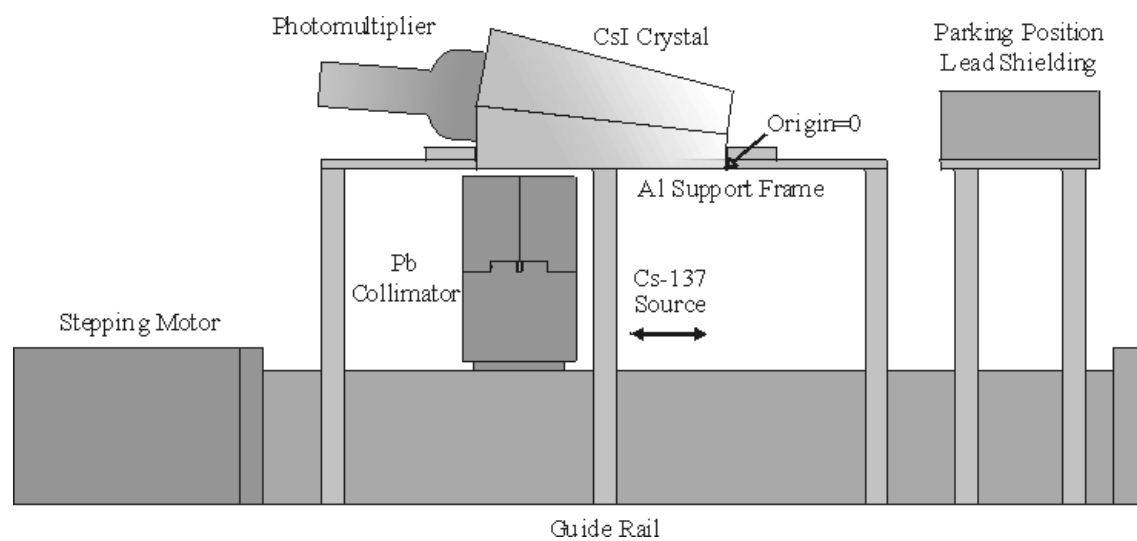


FIGURE 5



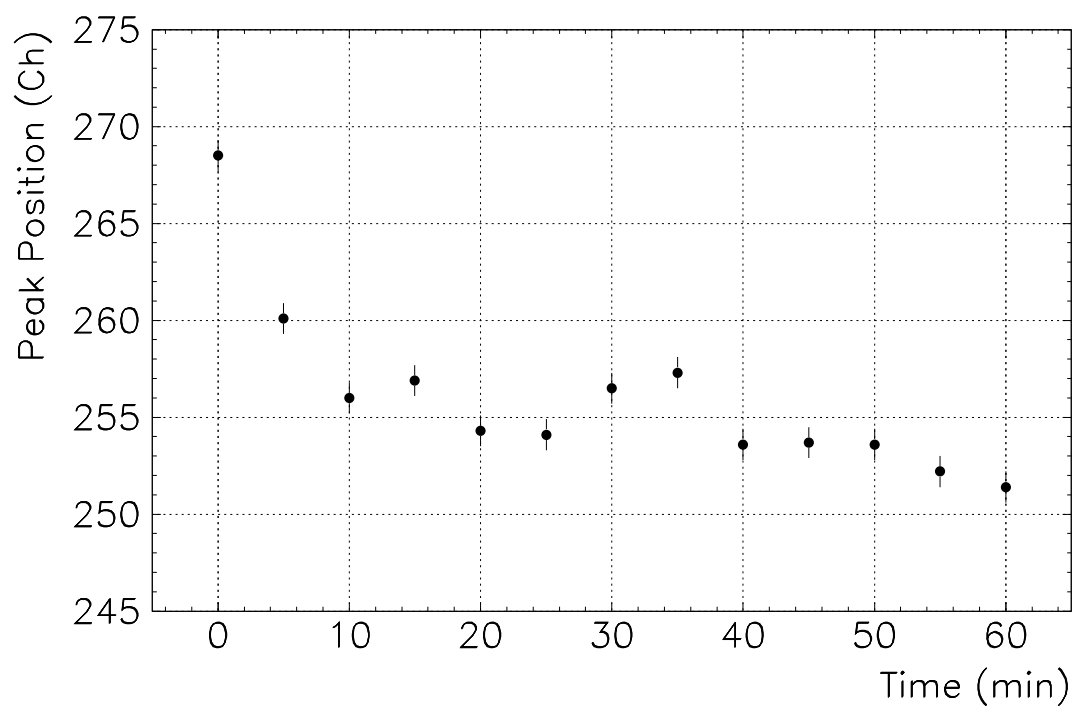


FIGURE 7

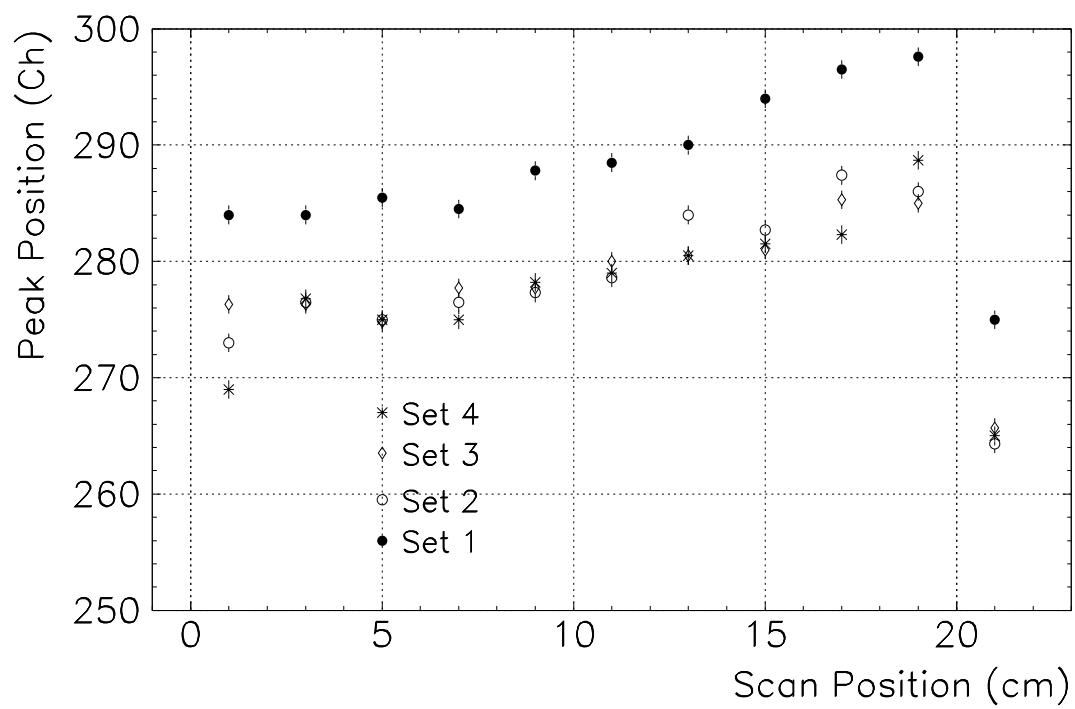


FIGURE 8

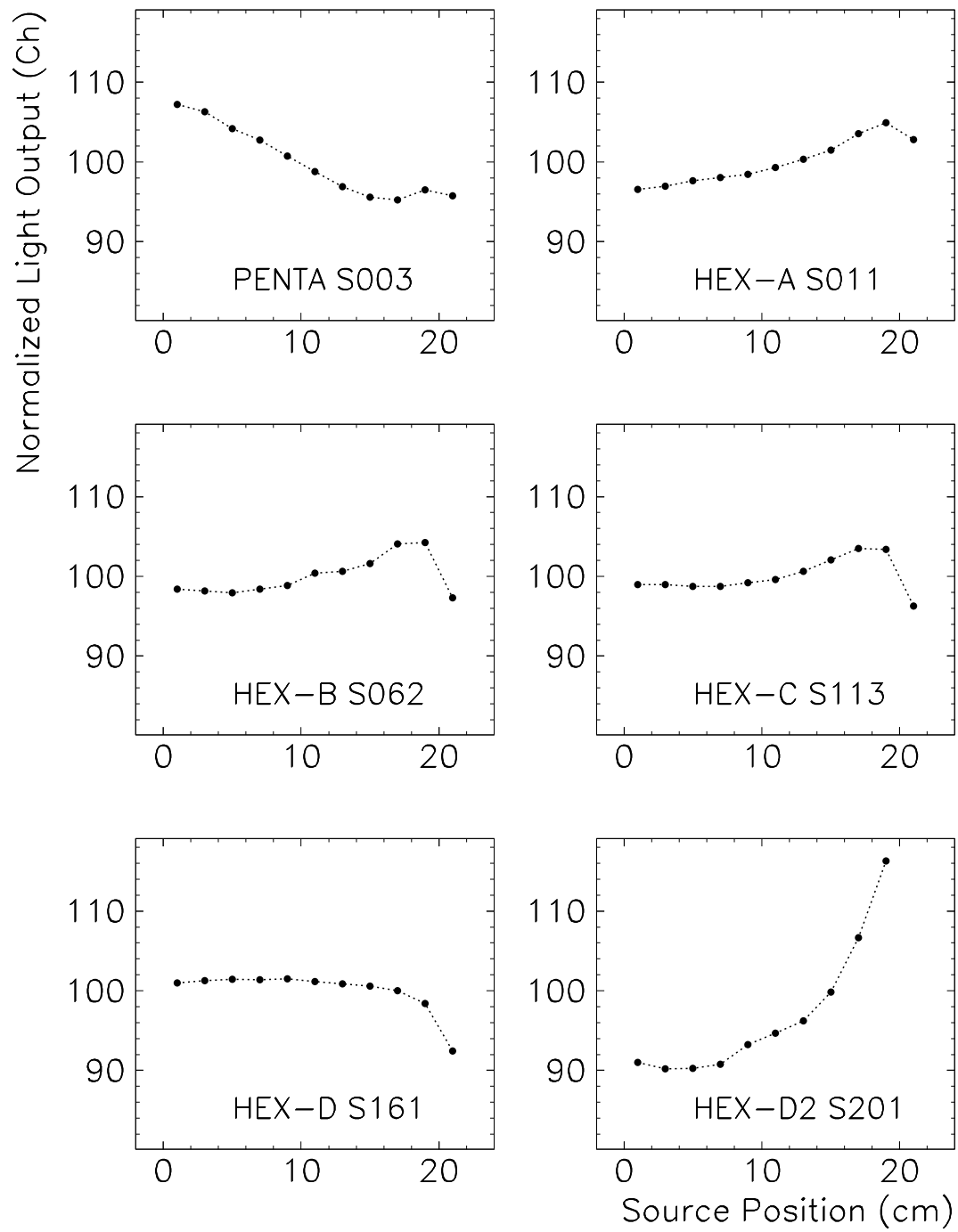


FIGURE 9

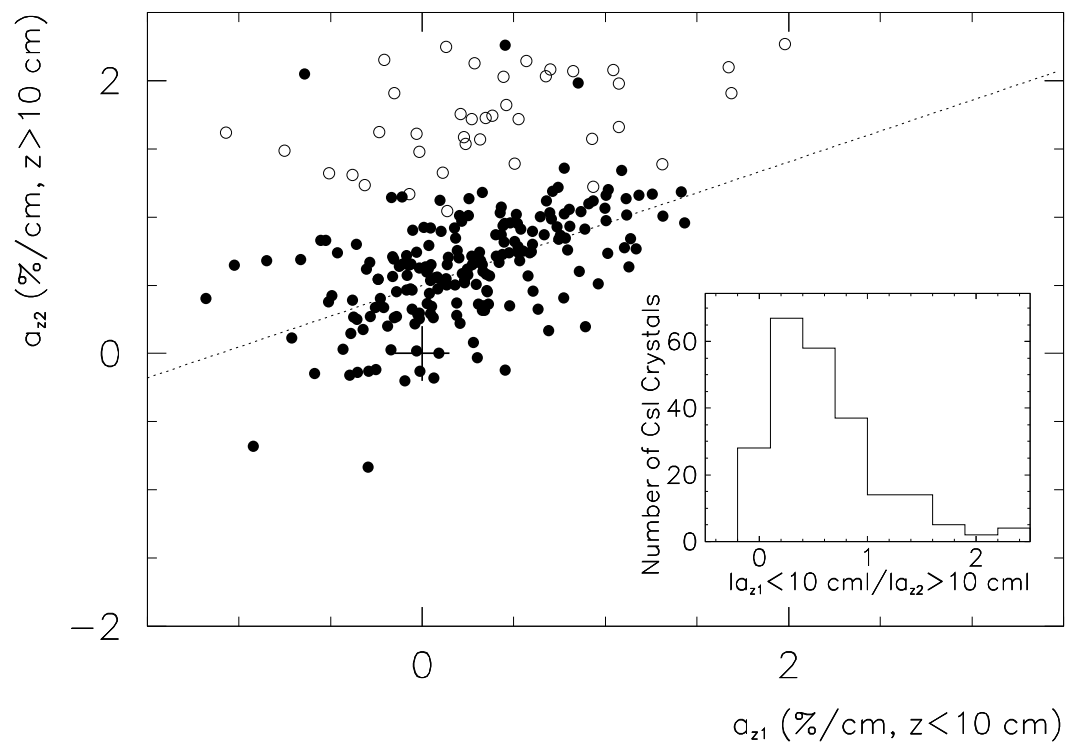


FIGURE 10

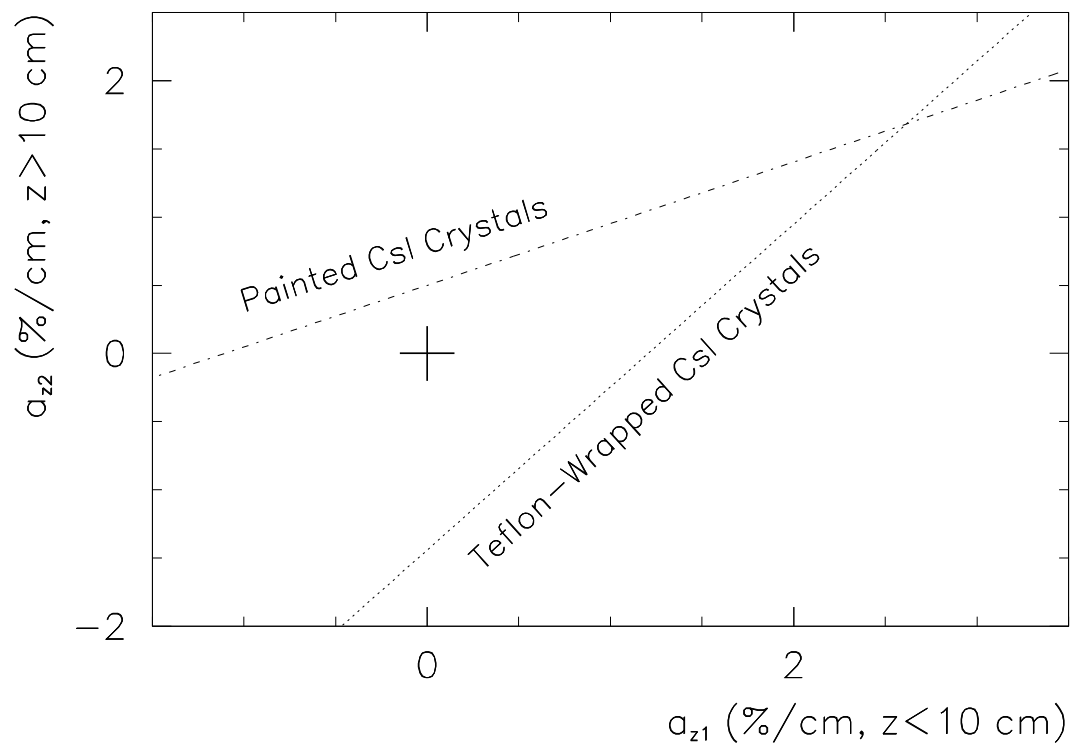


FIGURE 11

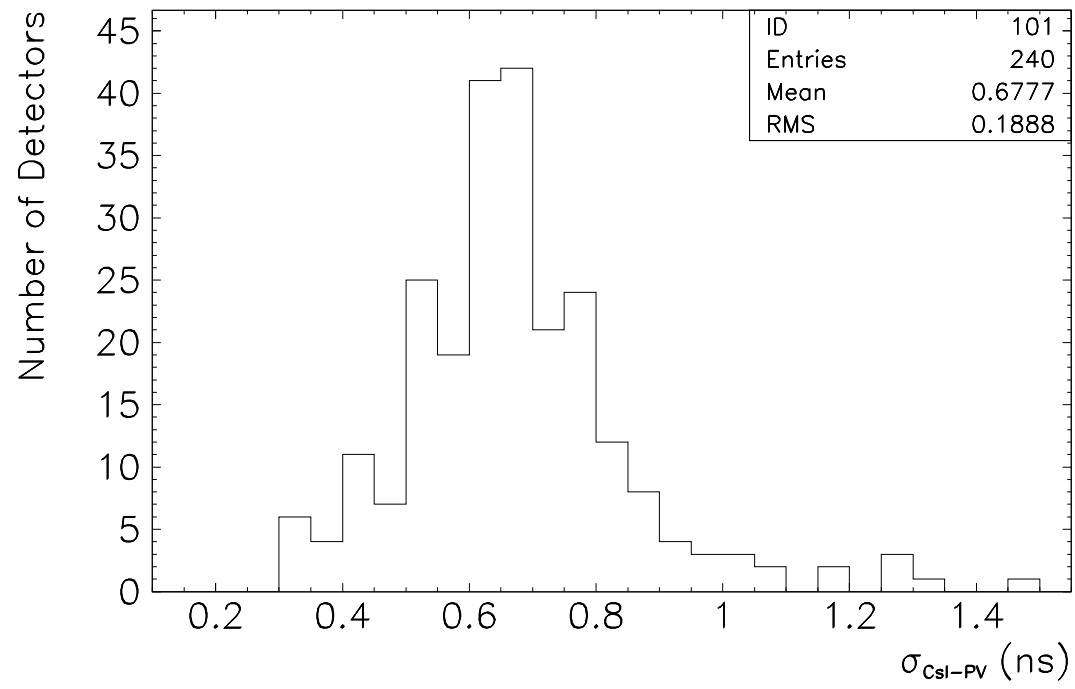
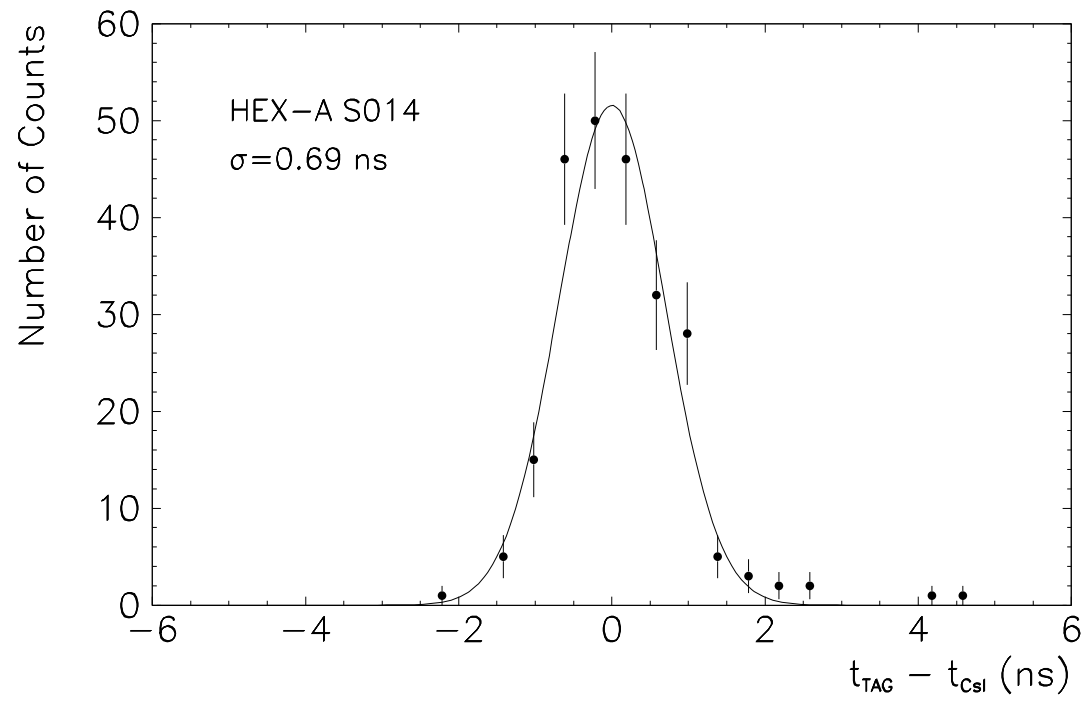


FIGURE 12

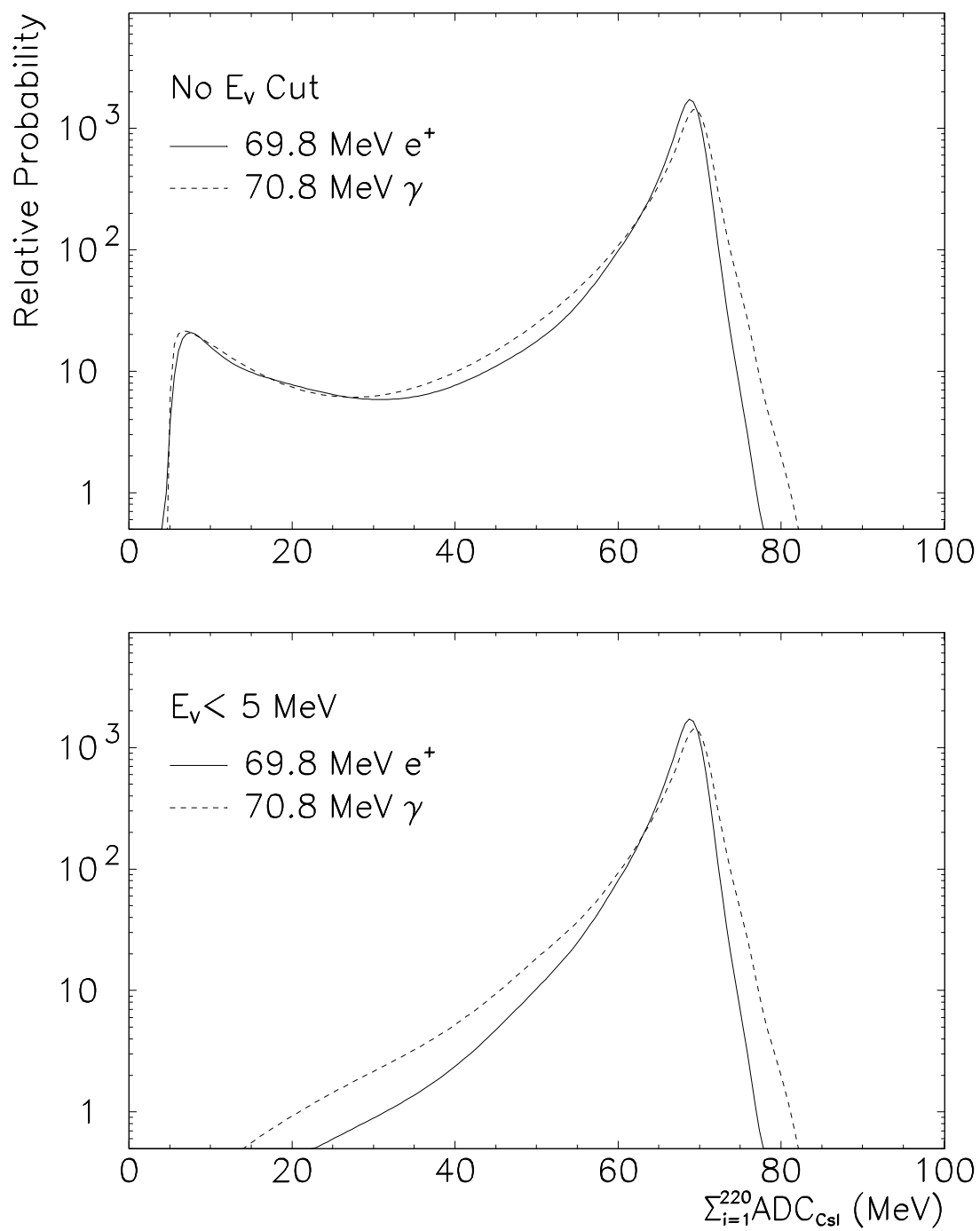


FIGURE 13

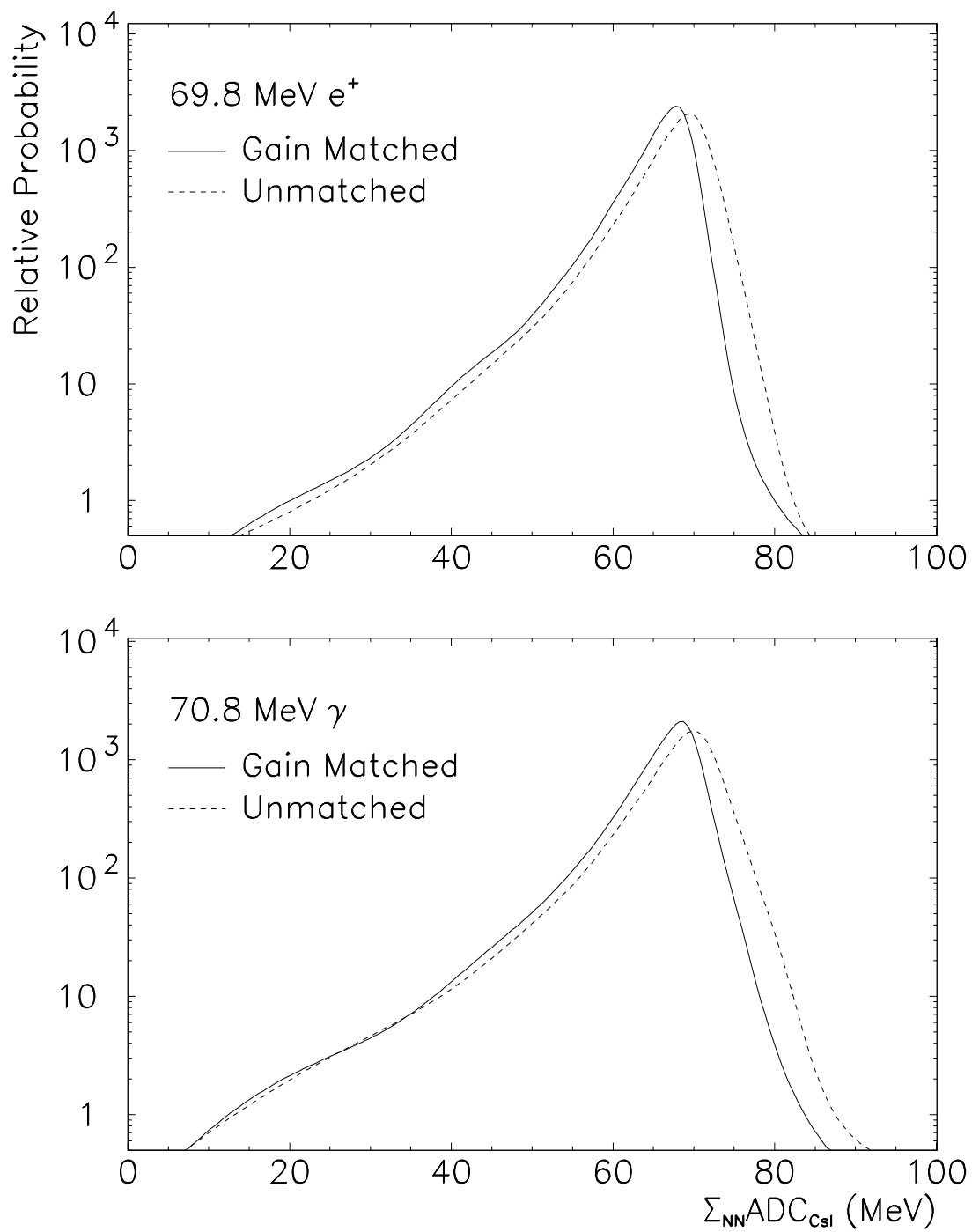


FIGURE 14

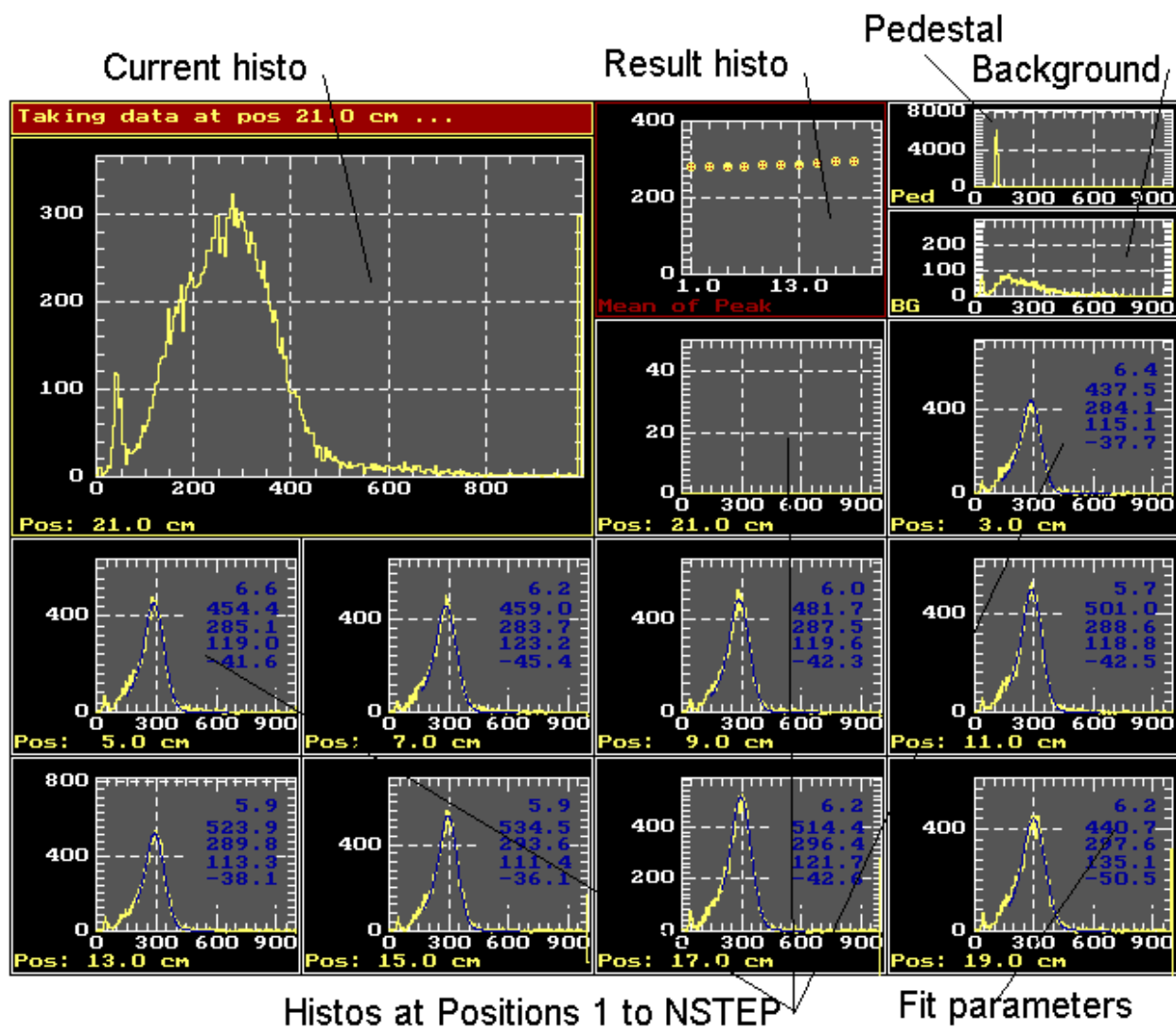


FIGURE 15